

# POST-MERGER SIGNATURES OF RED-SEQUENCE GALAXIES IN RICH ABELL CLUSTERS AT $z \lesssim 0.1$

YUN-KYEONG SHEEN<sup>1, 3</sup>, SUKYOUNG K. YI<sup>1, 4</sup>, CHANG H. REE<sup>2</sup>, JAEHYUN LEE<sup>1</sup>

*Draft version July 24, 2012*

## ABSTRACT

We have investigated the post-merger signatures of red-sequence galaxies in rich Abell clusters at  $z \lesssim 0.1$ : A119, A2670, A3330 and A389. Deep images in  $u'$ ,  $g'$ ,  $r'$  and medium-resolution galaxy spectra were taken using MOSAIC 2 CCD and Hydra MOS mounted on a Blanco 4-m telescope at CTIO. Post-merger features are identified by visual inspection based on asymmetric disturbed features, faint structures, discontinuous halo structures, rings and dust lanes. We found that  $\sim 25\%$  of bright ( $M_r < -20$ ) cluster red-sequence galaxies show post-merger signatures in four clusters consistently. Most ( $\sim 71\%$ ) of the featured galaxies were found to be bulge-dominated, and for the subsample of bulge-dominated red-sequence galaxies, the post-merger fraction rises to  $\sim 38\%$ . We also found that roughly 4% of bulge-dominated red-sequence galaxies interact (on-going merger). A total of 42% (38% post-merger, 4% on-going merger) of galaxies show merger-related features. Compared to a field galaxy study with a similar limiting magnitude (van Dokkum 2005), our cluster study presents a similar post-merger fraction but a markedly lower on-going merger fraction. The merger fraction derived is surprisingly high for the high density of our clusters, where the fast internal motions of galaxies are thought to play a negative role in galaxy mergers. The fraction of post-merger and on-going merger galaxies can be explained as follows. Most of the post-merger galaxies may have carried over their merger features from their previous halo environment, whereas interacting galaxies interact in the current cluster in situ. According to our semi-analytic calculation, massive cluster haloes may very well have experienced tens of halo mergers over the last 4–5 Gyr; post-merger features last that long, allowing these features to be detected in our clusters today. The apparent lack of dependence of the merger fraction on the clustocentric distance is naturally explained this way. In this scenario, the galaxy morphology and properties can be properly interpreted only when the halo evolution characteristics are understood first.

*Subject headings:* catalogs – galaxies: clusters: individual (Abell 119, Abell 2670, Abell 3330, Abell 389) – galaxies: evolution – galaxies: formation – galaxies: structure

## 1. INTRODUCTION

The formation of massive early-type galaxies in the universe is still in question. The hierarchical galaxy formation scenario is widely accepted at present, which predicts that massive galaxies form through hierarchical galaxy mergers. If each galaxy merger induces star formation and consequent stellar mass growth in the united galaxy, it would lead to a large scatter in the age and metallicity of stellar populations in massive early-type galaxies. However, the observational characteristics of early-type galaxies, such as their red colors tightly correlated in optical color-magnitude relations (CMRs) and their high  $\alpha$ –elements ratios, imply that most of the stellar contents in massive early-type galaxies formed in a short timescale at an early epoch ( $z > 1$ ). Furthermore, the red-sequence in the optical CMR appears to be established by  $z \sim 1$  (Tanaka et al. 2005), and recent observations with 8–10m-class telescopes reveal the appearance of massive red-sequence galaxies ( $M \gtrsim 10^{11} M_\odot$ ) at  $z \sim 2 - 3$  (Kodama et al. 2007; Drory & Alvarez 2008; Kang & Im 2009). These observational results suggest that most

massive early-type galaxies had almost completed their star formation and mass aggregation by  $z \sim 1$  and then virtually passively evolved.

There are other observational clues which indicate a significant increase in the stellar mass density in massive red-sequence galaxies since  $z \sim 1$ , which is not allowed according to the passive evolution of blue galaxies alone. Bell et al. (2004) showed that the  $B$ -band luminosity density of massive red-sequence galaxies does not evolve much in the redshift range of  $0 < z \leq 1.1$ . Because the  $B$ -band light should dim as stars get old, they argued that some young populations should be provided regularly from blue galaxies to the red-sequence during this period. However, the simple fading of massive blue galaxies cannot be applied, as the brightest red galaxy is always brighter than the brightest blue galaxy throughout the redshift range. After all, they suggested that galaxy mergers are an important process in the formation of luminous red galaxies since  $z \sim 1$ . The result was supported again by Faber et al. (2007).

Residual star formation (RSF) in early-type galaxies provides another clue about galaxy formation. RSF has been extensively studied, recently using the UV data from space telescopes such as the Galaxy Evolution Explore (*GALEX*) and the Hubble Space Telescope (*HST*). The latest work on the UV upturn phenomenon of early-type galaxies showed that RSF fraction among cluster elliptical galaxies is as high as  $\sim 30\%$ ; it is even

<sup>1</sup> Department of Astronomy and Yonsei University Observatory, Yonsei University, Seoul 120-749, Republic of Korea

<sup>2</sup> Korea Astronomy & Space Science Institute, Daejeon, 305-348, Republic of Korea

<sup>3</sup> Current address: Departamento de Astronomía, Universidad de Concepción, Casilla 160-C, Concepción, Chile

<sup>4</sup> Corresponding author: yi@yonsei.ac.kr

higher in the field environment (Yi et al. 2011). Several studies have claimed that the RSF in early-type galaxies is most likely related to galaxy mergers or interactions (Kaviraj et al. 2007; Kaviraj 2010b). Because the UV bright phase of a young stellar population lasts only  $\sim 1$  Gyr, we can estimate that the RSF detected at less than  $z = 0.1$  is stimulated at a relatively low redshift,  $z \sim 0.2 - 0.3$ . Again, this is indirect evidence of the substantial frequency of galaxy mergers given a low redshift.

van Dokkum (2005) showed tidally disturbed features around field elliptical galaxies at  $z \sim 0.1$  with optically deep images from NDWFS (NOAO Deep Wide Field Survey) and MUSYC (Multi-wavelength Survey of Yale and Chile). That paper suggested that  $\sim 70\%$  of field elliptical galaxies were assembled through dry mergers (i.e., mergers of gas-poor, bulge-dominated systems) in the recent epoch. Kaviraj (2010a) also found disturbed features as well as dust lanes from 25% of luminous early-type galaxies ( $M_r < -20.5$ ,  $z < 0.05$ ) in the ‘Strip 82’ fields of Sloan Digital Sky Survey (SDSS) data, which have much longer integration times than general SDSS fields. These are very meaningful results because mass growth via continuous galaxy mergers were up to that point mostly supported observationally by statistical analyses of photometric colors instead of by visual evidence of galaxy mergers. Moreover, the merger fraction is often estimated from galaxy pair fractions, considering them as pre-mergers (e.g., Bundy et al. 2009; de Ravel et al. 2009). Although van Dokkum (2005) and Kaviraj (2010a) did not deal with complete volume-limited samples, they searched a substantial number of galaxies with unprecedentedly deep optical images and presented direct evidence of galaxy mergers related to the formation of red, early-type galaxies.

Our interest moved to galaxy clusters, which are dominated by massive early-type galaxies. It has been expected that galaxy clusters are not a likely environment for frequent merger events to take place due to the high peculiar motions of the galaxies within the cluster. Moreover, it is commonly held that massive galaxies in clusters formed faster at an earlier epoch than did galaxies in a field environment (Gunn & Gott 1972; Dressler 1980; Tanaka et al. 2005 and references in it). Therefore, it was presumed that it would be difficult to find post-merger signatures from massive early-type galaxies in galaxy clusters. Naturally, there has been less effort to find post-merger signatures among cluster galaxies.

To find post-merger signatures of early-type galaxies in galaxy clusters, we carried out optical deep imaging and multi-object spectroscopic observations of four rich Abell clusters at  $0.04 < z < 0.11$  with the Blanco 4-m telescope at the Cerro Tololo Inter-American Observatory (CTIO). We picked four rich Abell clusters (A119, A2670, A3330 and A389) as our targets. They have been observed by GALEX at least in the medium-depth imaging mode (MIS: Medium Imaging Survey) and are optimally visible from the CTIO. Their GALEX NUV exposure times range from  $\sim 1$  hours for A119 to  $\sim 17$  hours for A3330. UV light is very sensitive to the existence of young stellar populations and thus plays an important role in the study of the recent star formation history that may have been caused by mergers. The UV properties will be published in an upcoming paper following this one, in which we initially present the optical colors

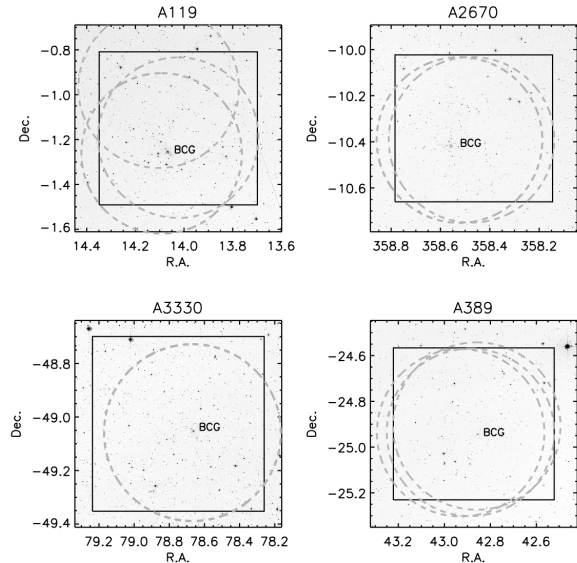


FIG. 1.— The field-of-views of the MOSAIC2 and Hydra data are superimposed over the DSS image for each cluster. The square in each panel indicates the field of the stacked deep image while the gray-dashed circles represent the observed Hydra FOVs. Their consistent FOVs enabled us to perform an almost complete spectroscopic survey of the cluster galaxies.

and morphologies of cluster galaxies. We performed a visual inspection of all the red-sequence galaxies brighter than  $M_r = -20$  in each galaxy cluster using deep optical images. This result will enable us to compare the recent galaxy merger histories between cluster and field environments. Morphological indexes such as the bulge-to-total ratio and asymmetry of the galaxies were also measured to examine their morphological characteristics.

In this paper, the observations and data reductions are presented in Section 2 and Section 3. Section 4 describes the galaxy sample selection process and Section 5 shows the scheme and the result of the visual inspection using the deep optical images. Morphological examination will be presented in Section 6. We will conclude this paper with a summary and discussion in Section 7.

## 2. OBSERVATIONS

Deep optical images of the Abell clusters were taken with the MOSAIC 2 CCD mounted on the Blanco 4-m Telescope at CTIO. Medium-resolution spectra ( $R \sim 1000$ ) of galaxies in the cluster fields were acquired with Hydra, a multi-object spectrograph on the Blanco. Observations were performed three times through 2006 – 2008. The target clusters and acquired data are summarized in Table 1. Only the short exposure image ( $t_{exp} = 600$  sec) of A389 was taken separately in early 2009 with the same telescope and instrument. MOSAIC 2 consists of eight  $2K \times 4K$  CCDs (therefore, the overall dimension is  $8K \times 8K$  pixels), and Hydra utilizes a  $2K \times 4K$  CCD. The pixel scale of MOSAIC 2 is  $0.24''/\text{pixel}$  after the astrometry is done. MOSAIC 2 has a  $36' \times 36'$  field-of-view (FOV) and Hydra has a circular FOV that is  $40'$  in diameter. The FOVs of MOSAIC 2 and Hydra are plotted over Digitized Sky Survey images in Figure 1 for each cluster. The square in each panel indicates the region of the stacked deep image while the gray-dashed circles represent FOVs of Hydra observations. Their consistent

TABLE 1  
CTIO OBSERVATIONS SUMMARY

Cluster ID	RA(J2000)	Dec(J2000)	Instrument	Filter	$t_{exp}$ (sec) <sup>a</sup>	# of pointing <sup>b</sup>	Date
Abell 119 ( $z \sim 0.044$ )	00:56:21.4	-01:15:47	MOSAIC 2	$u'$	6000 / 1200	5	27,29 Oct. 2008
				$g'$	5760 / 120	8	
				$r'$	5760 / 120	8	
			Hydra		9000	4	6–11 Nov. 2008
Abell 2670 ( $z \sim 0.076$ )	23:54:10.1	-10:24:18	MOSAIC 2	$u'$	4800 / 700	6	13,15 Nov. 2007
				$g'$	5100 / 200	6	
				$r'$	6000 / 60	6	
			Hydra		5400	3	27–29 Nov. 2007
Abell 3330 ( $z \sim 0.089$ )	05:14:40.0	-49:03:15	MOSAIC 2	$u'$	4600 / 460	10	26 Nov. 2006
				$g'$	5000 / 200	10	
				$r'$	6150 / 100	15	
			Hydra		14400 / 3600 <sup>c</sup>	3/6	27–29 Nov. 2007 / 1–3 Dec. 2006
Abell 389 ( $z \sim 0.113$ )	02:51:31.0	-24:56:05	MOSAIC 2	$u'$	6000 / 1200	5	27,29 Oct. 2008
				$g'$	7200 / 1200	6	
				$r'$	7200 / 600	6	
			Hydra		10800	3	6–11 Nov. 2008

<sup>a</sup> The first numbers are the total exposure time of the stacked images and the second numbers represent the short exposure images that were analyzed.

<sup>b</sup> The numbers indicate the number of dithering points for imaging and the number of fiber configurations for spectroscopy for each target field.

<sup>c</sup> Spectroscopic redshifts of some A3330 galaxies were complemented by the spectra taken in 2006.

FOVs enabled us to perform an almost complete spectroscopic survey of the cluster galaxies effectively.

All of the deep images were taken on dark nights (moon illumination  $< 0.4$ , the average is 0.17) while the spectroscopic observations were performed on bright nights. The imaging nights were usually photometric and the average seeing was less than  $1''$  during the entire period of observation. We obtained the deep images with  $u'$ ,  $g'$ ,  $r'$  filters in the Blanco telescope. In order to fill the gap between the eight chips in the MOSAIC 2 CCD, more than five points of dithering was applied for each filter. The maximum number of dithering points was 15 for the  $r'$  band deep image of Abell 3330. The  $u'g'r'i'z'$  standard stars in Chandra Deep Field South(CDF-S, Smith et al. 2003) were also observed every night to standardize the photometric data.

Hydra observations were performed with a KPGL3 grating centered at 5205Å. A blocking filter, GG385, was also used to suppress the bluer wavelength below 3850Å. The resolving power was  $R \sim 1100$  at 5500Å and the dispersion was 1.40Å/pixel after binning two pixels along the dispersion axis. Calibration frames were taken with a “Penray” lamp for wavelength calibration and with a “Quartz” lamp as an aperture reference. We used the 138 large fibers available in Hydra. The fiber width was 300  $\mu\text{m}$ , which correspond to  $2''$  in the sky. In a fiber configuration,  $\sim 100$  fibers were assigned for galaxies while  $\sim 10$  fibers were allocated to blank sky for the sky spectra. Three to four fiber configurations were designed for each galaxy cluster for the possible cluster members not to be missed by fiber collisions and the limited number of fibers. Every fiber configuration was also taken through three separate exposures for median combine for data reduction purposes.

### 3. DATA

#### 3.1. MOSAIC 2 photometric data

#### 3.1.1. Data reduction

The MOSAIC 2 data are mainly reduced using the **mscred** package in IRAF. All of the calibration data described in this section were obtained for every run and were applied to the object frames observed during the same run. First, we updated the characteristic information of each CCD chip. New crosstalk files were generated with the **xtcoeff** task using shallow object frames which have saturated stars upon a small sky background for the CCD pairs of MOSAIC 2. Doing this corrects the ghost images of saturated stars reflected onto each other between a pair of CCDs. Gains and readout noises of eight chips were computed with the **mscfndgain** task. In addition, the bad pixel mask of each chip was revised manually via visual inspection. We then updated all of the FITS files of the same observing run with the new information. An IRAF task **ccdproc** handled all of the pre-processes at once, such as crosstalk correction, bad pixel mask correction, overscan strip correction, image trim, bias correction, and flat-fielding. The combined dome flats were used for the flat-fielding of  $g'$ ,  $r'$  band images, while the combined sky flat was used for the  $u'$  band images.

Once the pre-process was done, we found a smooth background gradient in the  $g'$ ,  $r'$  band deep images. Illumination correction was carried out for each band using the dark-sky flats generated from the object-subtracted deep images. After illumination correction, the deep images showed  $\pm 2\%$  deviation in their background over the field of each frame. Cosmic rays were removed from all of the long-exposure images ( $t_{exp} \geq 500$  sec) using the **lacosmic** routine (van Dokkum 2001). Satellite trails occasionally appeared in the long exposures. They were erased using the **satzap** task.

Object frames were stacked to a single deep image in each band. The stacking procedure followed the general guide of the National Optical Astronomy Observatory MOSAIC data reduction (Jannuzi, Claver & Valdes

2003). Astrometry was carried out very carefully for every chip using the `msctpeak` task in IRAF to achieve positional errors of less than 0.3'' in RMS (Readers are referred to Valdes 2000 for details).

### 3.1.2. Standardization

Standardization equations were derived for each observing run with  $u'g'r'i'z'$  standard stars in CDF-S (Smith et al. 2003). Basically, optical photometry in the  $g'$ ,  $r'$  band had to be performed using shallow images ( $t_{exp} \sim 100$  sec), as we had intentionally saturated the galactic centers in the deep images to see the faint structures around the galaxies. Only for A389, the farthest galaxy cluster among our target clusters, did we use a single deep image ( $t_{exp} = 1200$  sec) and a relatively short exposure ( $t_{exp} = 600$  sec) for  $g'$  and  $r'$  band photometry, respectively. The standardization equations were established for the nights in which the short exposures were taken.

The eight chips of MOSAIC 2 CCD have slightly different characteristics in terms of photon efficiency. Therefore, great care was required when measuring the brightness from different chips for consistency. For this reason, we tried to allocate standard stars to the greatest extent possible in one chip and derived the standardization equations using the standard stars in it. Chip 6 of the MOSAIC 2 CCD was dedicated to this work because it has the deepest electron-capacity among the eight chips. Stars with small photon-statistical errors ( $< 0.03$  mag) were used in the calculations. As a result, 7  $\sim$  9 stars were available for the standardization of the  $g'$ ,  $r'$  band data and 6 stars were available for the  $u'$  band data among the 22 standard stars listed in Smith et al. (2003). Instrumental magnitudes were measured with a fixed aperture diameter, 14''.86, which is adopted from Smith et al. (2003). Because the aperture diameter is already larger than  $7 \times \text{FWHM}$  in our data (typical  $\text{FWHM} \lesssim 1''$ ), we did not consider aperture correction in the photometry of standard stars.

Standardization equations were established as follows:

$$u' = u'_{inst} + a_{u'} + b_{u'}X_{u'} + c_{u'}(u' - g') \quad (1)$$

$$g' = g'_{inst} + a_{g'} + b_{g'}X_{g'} + c_{g'}(g' - r') \quad (2)$$

$$r' = r'_{inst} + a_{r'} + b_{r'}X_{r'} + c_{r'}(g' - r') \quad (3)$$

The  $u'g'r'$  magnitudes in the above equations are the standard magnitudes and the instrumental magnitudes are defined as  $m_{inst} = -2.5 \times \log(\text{counts(ADU/sec)}) + 25$ .  $X$  is an effective airmass of each object frame. Initially, the basic offsets between the standard magnitudes and the instrumental magnitudes were calculated and corrected for the instrumental magnitudes. The magnitudes were then fitted versus the airmass. The fitting function provided the relationship with which to determine the airmass term in the standardization equations. In the same manner, we fitted the airmass-corrected magnitudes versus the optical colors and determined the color terms in the equations. Weighted-mean values are used throughout the fitting process. The coefficients of standardization equations are presented in Table 2.

The standardization equations were applied to the instrumental magnitudes from short exposure images to determine the standard magnitudes of galaxies. We then

TABLE 2  
STANDARDIZATION COEFFICIENTS

Date	Filter	$a$	$b$	$c$
2006 Nov 26	$u'$	$-1.478 \pm 0.064$	$-0.441 \pm 0.009$	$0.126 \pm 0.048$
	$g'$	$1.002 \pm 0.012$	$-0.168 \pm 0.005$	$0.002 \pm 0.020$
	$r'$	$0.982 \pm 0.005$	$-0.088 \pm 0.002$	$-0.018 \pm 0.007$
2007 Nov 13	$u'$	$-1.385 \pm 0.086$	$-0.399 \pm 0.018$	$0.078 \pm 0.064$
	$g'$	$1.028 \pm 0.021$	$-0.139 \pm 0.012$	$-0.049 \pm 0.029$
	$r'$	$1.001 \pm 0.012$	$-0.087 \pm 0.007$	$-0.032 \pm 0.014$
2008 Oct 29	$u'$	$-1.288 \pm 0.064$	$-0.526 \pm 0.011$	$0.095 \pm 0.048$
	$g'$	$1.119 \pm 0.013$	$-0.228 \pm 0.007$	$-0.113 \pm 0.020$
	$r'$	$1.054 \pm 0.006$	$-0.155 \pm 0.003$	$-0.041 \pm 0.009$

TABLE 3  
THE AVERAGE OF  $k$ -CORRECTION TERMS

Cluster	$K_{u'}$	$K_{g'}$	$K_{r'}$
A119	$-0.20 \pm 0.03$	$-0.11 \pm 0.02$	$-0.04 \pm 0.01$
A2670	$-0.29 \pm 0.06$	$-0.19 \pm 0.03$	$-0.07 \pm 0.02$
A3330	$-0.34 \pm 0.06$	$-0.24 \pm 0.04$	$-0.09 \pm 0.02$
A389	$-0.42 \pm 0.06$	$-0.32 \pm 0.05$	$-0.13 \pm 0.03$

derived the standardization constants for the  $u'g'r'$  deep images using the standard magnitudes determined earlier. The offsets between the standard magnitudes and the instrumental magnitudes from the deep images were calculated with non-saturated stars using aperture photometry. A typical standard deviation of the standardization constants (the average of magnitude offsets) was  $\lesssim 0.001$  mag.

### 3.1.3. Photometry

The optical magnitudes of the galaxies were measured with SExtractor from the MOSAIC 2 data and calibrated as described in Section 3.1.2. Essentially, we adopted Auto\_Magnitude (`MAG_AUTO`) of SExtractor (Bertin & Arnouts 1996) as the representative galaxy magnitude.

Galactic foreground extinction was corrected using the reddening maps from Schlegel et al. (1998). The  $E(B - V)$  value applied to each cluster is 0.039, 0.042, 0.028, and 0.016 for A119, A2670, A3330, and A389, respectively. Finally,  $k$ -correction was performed by means of simple two-population (old plus young) modeling on the UV-optical continua from photometry consisting of *GALEX* FUV, NUV and CTIO  $u'$ ,  $g'$ ,  $r'$  bands. In the modeling, the old population has a fixed age of 12 Gyr and the young component varies in age ( $0.01 \text{ Gyr} \leq t_{young} \leq 10 \text{ Gyr}$ ) and mass fraction ( $10^{-4} \leq f_{young} \leq 1$ ). Section 3 in Yi et al. (2011) details the procedure. The average of the  $k$ -correction values for the cluster red-sequence galaxies are presented for each galaxy cluster in Table 3. The  $k$ -corrected magnitudes are used in all of the analyses in this paper.

The distance moduli used for the absolute magnitudes calculations are 36.25, 37.46, 37.88, and 38.32 for A119, A2670, A3330, and A389, respectively.

### 3.2. Hydra spectroscopic data

Hydra spectroscopic data were reduced using the `hydra` package in IRAF. First, the  $2K \times 2K$  images (after binning along the dispersion axis) were pre-processed

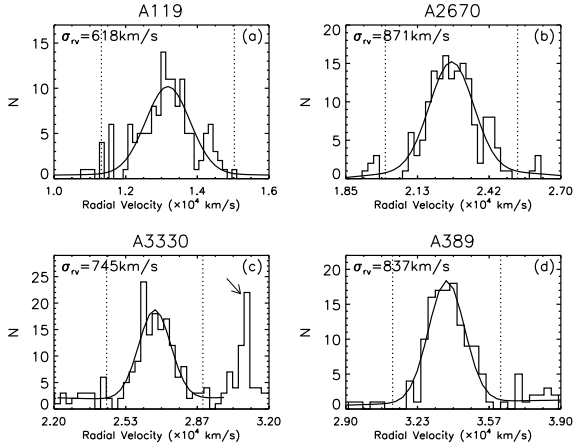


FIG. 2.— Radial velocity histogram of the galaxy clusters. The Gaussian fits are plotted over the histograms. The dotted lines indicate the velocities of  $v_{r,center} \pm 3\sigma_{v_r}$ , with which cluster members are selected. The arrow in the panel (c) indicates a background cluster of Abell 3330 which appears in Section 4.2.

to flat-fielding as with the imaging data. After the preprocesses, spectral apertures were traced from the two-dimensional images and fiber-to-fiber throughput variation was corrected with a combined sky flat taken in each observing run. Wavelength calibration and sky subtraction were also carried out. The procedures after preprocessing were performed via the `dohydra` task. All of the spectra were taken in three separate exposures for median combine. To combine the spectra, we normalized each spectrum using the `continuum` task, after which three spectra of a galaxy were combined into one spectrum with the `scombine` task.

Galaxy radial velocities were measured from the combined spectra using the `fxcor` task in IRAF, which adopts a cross-correlation method between a rest-frame galaxy spectral template and a galaxy spectrum (Tonry & Davis 1979). The early-type galaxy template and the luminous red galaxy template from SDSS were utilized for our radial velocity measurement, as we primarily targeted red-sequence galaxies in the Hydra observations.

#### 4. GALAXY SAMPLE SELECTION

##### 4.1. Cluster memberships

Cluster memberships are determined by spectroscopic redshifts of galaxies. We measured the radial velocity dispersion ( $\sigma_{v_r}$ ) of the cluster galaxies with the Hydra spectra. Because A2670 and the northern half of A119 are observed by SDSS, we included the SDSS spectra of galaxies which we had missed in the Hydra observations. Radial velocity distributions from the combined catalogs (Hydra observations + SDSS archive) are shown in Figure 2. The bin sizes are determined as one hundredth of the central velocities of the galaxy clusters. The center and dispersion of the radial velocity distributions are determined using a Gaussian fitting IDL code, `gaussfit`. The fitting result is plotted over the histogram with a solid curve. The central velocities and velocity dispersions of the cluster galaxies are presented in Table 4. Cluster memberships are assigned to the galaxies included within  $\pm 3\sigma_{v_r}$  from the cluster central velocity. In Figure 2, the dotted lines mark the velocity ranges of the cluster memberships. As a result, we identified

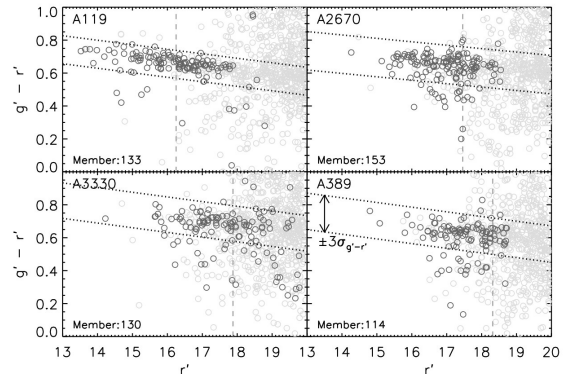


FIG. 3.— Optical color-magnitude relationships of the four target clusters with the MOSAIC 2 data. The dark-gray open circles indicate the spectroscopic members while the bright-gray open circles present all of the galaxies from the field of deep optical images. Red-sequences are defined by iterative linear fitting with the spectroscopic member galaxies. The dotted lines in each panel indicate the  $\pm 3\sigma$  boundaries from the best fit. We defined the red-sequences with galaxies within the boundaries. The luminosity cut ( $M_{r'} = -20$ ) for this study is indicated with a gray dashed line in each CMR.

133, 153, 130 and 114 member galaxies for A119, A2670, A3330 and A389, respectively. Among them, 32 and 39 galaxies are supplemented from the SDSS spectroscopic data for A119 and A2670.

To estimate  $R_{200}$  from the velocity dispersion, we adopted equation (8) of Carlberg et al. (1997). With the assumption of that density profile is a singular isothermal sphere in the target clusters,  $R_{200}$  can be defined as,

$$R_{200} = \frac{\sqrt{3}}{10} \frac{\sigma}{H(z)}. \quad (4)$$

The  $\sigma$  is the characteristic velocity dispersion of a galaxy cluster. In our calculation, we employed the  $\sigma_{v_r}$  from the Gaussian fit of each galaxy cluster for the  $\sigma$ . The Hubble constant,  $H_0 = 70 \text{ km s}^{-1} \text{ Mpc}^{-1}$ , is applied to the equation instead of the Hubble parameter,  $H(z)$ , assuming no evolution of  $H$  in the redshift range,  $0 < z \leq 0.1$ . As a result,  $R_{200}$  is estimated as 1.53, 2.16, 1.84, and 2.07 Mpc for A119, A2670, A3330, and A389, respectively. The MOSAIC 2 CCD does not cover the entire region of the galaxy clusters. The general width of a side of a stacked deep image is  $36'$ , which corresponds to 1.9, 3.1, 3.6, and 4.4 Mpc at distances of A119, A2670, A3330, and A389, respectively. If it is assumed that a cluster center is located in the center of a deep image, the images cover 62% (0.95/1.53), 72% (1.55/2.16), 98% (1.8/1.84), and 106% (2.2/2.07) of  $R_{200}$  for each galaxy cluster.

With  $R_{200}$ , we estimated the mass of the clusters as well. All of the target clusters were more massive than  $2 \times 10^{14} M_\odot$ . The mass of A2670 was  $\sim 7.3 \times 10^{14} M_\odot$ , proving that it is one of the most massive galaxy clusters in the universe.

##### 4.2. Red-sequence galaxies

Because our interest is focused on the formation of massive red galaxies in galaxy clusters, we defined a red-sequence in each galaxy cluster first. The optical color-magnitude relationships of the target clusters are presented in Figure 3. In the figure, the dark-gray open cir-

TABLE 4  
SPECTROSCOPIC PROPERTIES OF THE CLUSTERS

ID	$v_{r,center}$ (km/s)	$\sigma_{v_r}$ (km/s)	$z$	$R_{200}$ (Mpc)	$M_{200}$ ( $\times 10^{14} M_{\odot}$ )	# of spectroscopic members <sup>a</sup>
A119	$1.32 \times 10^4$	618	0.044	1.53	2.6	133 (32)
A2670	$2.27 \times 10^4$	871	0.076	2.16	7.3	153 (39)
A3330	$2.67 \times 10^4$	746	0.089	1.84	4.5	130
A389	$3.37 \times 10^4$	837	0.112	2.07	6.4	114

<sup>a</sup> The numbers in parenthesis indicate the number of member galaxies identified using SDSS data.

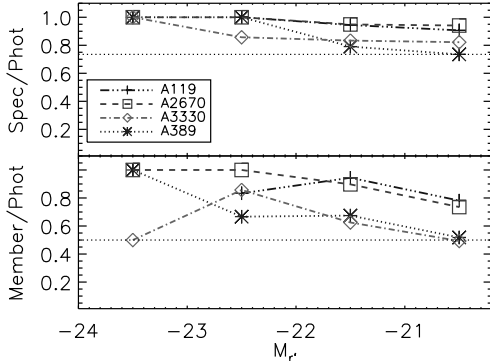


FIG. 4.— The top panel shows the spectroscopic completeness of our data for the red-sequence galaxies along the  $r'$  band absolute magnitudes. Although the spectroscopic coverage decreases as the galaxies become fainter, still more than 73% of the  $-21 \leq M_{r'} < -20$  photometric red-sequence galaxies are targeted. The bottom panel shows the spectroscopic member fractions among the photometric red-sequences along magnitude. The horizontal dotted lines mark 73% and 50% in the top and bottom panels, respectively, as the lowest fraction in each plot. With this plot, we learn that red-sequences are considerably contaminated by background/foreground galaxies even in the cluster fields.

cles indicate the spectroscopic members while the bright-gray open circles present all of the galaxies from the field of deep optical images. Though the red-sequences are distinctively revealed in the CMRs, we empirically defined red-sequences using the spectroscopically identified cluster members. However, it was not as simple as visual recognition of the sequences, as a red-sequence has a slight bend near the bright end of the sequence. Thus, we carried out two-step linear fitting by means of a  $2\text{-}\sigma$  clipping method. Initially, a preliminary fit was derived using data within a rectangle box which includes galaxies near the bright end of an apparent red-sequence. Once the preliminary fit appears to be close to the actual sequence, we calculated the standard deviation ( $\sigma_{g'-r'}$ ) of the data to the fit. Linear fitting was then performed again using the new data set confined by the new  $\pm 2\sigma_{g'-r'}$  color boundaries with  $r' < r'_{\text{brightest}} + 5$ . This two-step fitting process allowed us to obtain reasonable fitting results corresponding to what we observed in the CMRs. The zero points and slopes for the red-sequences in our targets clusters are  $1.107 \pm 0.079$  and  $-0.026 \pm 0.004$ , respectively. The small scatters are consistent with previous findings of universal red-sequences in galaxy clusters (Bower, Lucey & Ellis 1992; Stanford, Eisenhardt & Dickinson 1998). Using the final fits, the standard deviations were calculated again with the data within the  $\pm 2\sigma_{g'-r'}$  color boundaries. The final values were  $\sigma_{g'-r'} = 0.028, 0.039, 0.036$ , and  $0.037$  for A119, A2670, A3330, and A389. The red-sequences are defined

with galaxies within  $\pm 3\sigma_{g'-r'}$  using the final fits and standard deviations. The color boundaries are expressed in dotted lines in Figure 3.

We attempted to perform a complete spectroscopic survey of the red-sequence galaxies during the Hydra observations. The top panel in Figure 4 shows the spectroscopic completeness of our data for the red-sequence galaxies along the  $r'$  band absolute magnitudes. Although the spectroscopic coverage decreases as the magnitude becomes fainter, still more than 73% of the  $-21 \leq M_{r'} < -20$  photometric red-sequence galaxies are targeted. The bottom panel shows the spectroscopic member fraction in the red-sequences along the magnitudes. With the plot, we learn that red-sequences are considerably contaminated by background/foreground galaxies even in the cluster fields. In the case of A2670, though it has very high spectroscopic completeness for the faintest magnitude bin, the spectroscopic member fraction is in good agreement with the results from other clusters. Abell 3330 shows the low member fraction for the brightest magnitude bin in the bottom panel of Figure 4. It is due to the brightest cluster galaxy of a close background cluster in the field. The background cluster is indicated with an arrow in Figure 2 (c).

The absolute magnitude cut of  $M_r < -20$  is applied for the galaxy sample selection because beyond that, spectroscopic survey completeness is low and visual inspection is difficult for the galaxies at  $z \sim 0.1$ . Finally, our galaxy samples are defined by the spectroscopic members in the red-sequences; they are also brighter than  $M_r = -20$  in each galaxy cluster. We term the galaxy samples ‘RS<sub>sp</sub>’ throughout this paper.

## 5. VISUAL INSPECTION

### 5.1. The scheme

Our approach to find post-merger signatures involves a visual inspection of the galaxies with the MOSAIC 2  $r'$  band deep images. The faint surface brightness level of  $\mu_{r'} \sim 30$  mag/arcsec<sup>2</sup> is acquired in the deep images for all target clusters. The general Petrosian diameter along the major axis of the  $M_{r'} = -20$  galaxy is  $\sim 14.4''$  ( $\sim 60$  pixels) in the  $r'$  band deep images, corresponding to  $\sim 27$  kpc at  $z = 0.1$ . Generously assuming that a typical seeing is 1 arcsec, the spatial resolution is  $\sim 1.9$  kpc at this distance. This can be regarded as the worst condition for our visual inspection.

We attempted to establish the classification criteria for the visual inspection in a manner faithful to *how the galaxies appear* in the images. Therefore, the galaxies were classified as “Elliptical/S0” (E), “Post-merger” (PM), “Interacting” (I), “Pair” (P), “accompanying Faint Companions” (FC), and “Spiral” (S). “El-

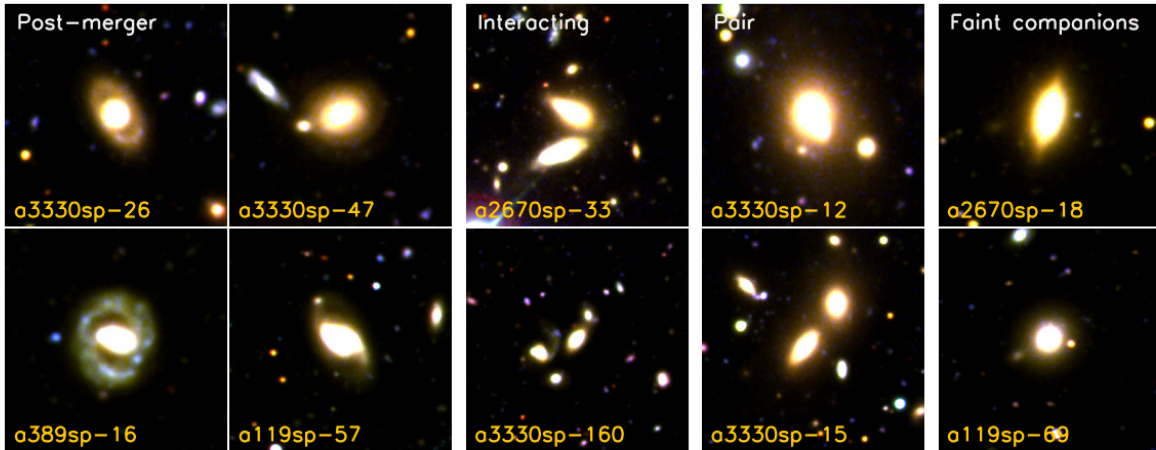


FIG. 5.— This figure shows galaxy examples along the classification scheme. The first two columns show post-merger (PM) galaxy examples and the examples of interacting galaxies (I), and pair (P), and faint companions (FC) are presented in the following columns.

lptical/S0” denotes the normal elliptical and lenticular galaxies without any disturbed features. Additionally, “Spiral” indicates normal spiral galaxies. “Post-merger” denotes galaxies showing disturbed features, e.g., asymmetric structures, faint features, discontinuous halo structure, rings and dust lanes. These are considered as galaxy merger remnants. “Interacting” galaxies also exhibit disturbed features as well as PM galaxies but they are close companions and interact with each other, i.e., they are on-going merger candidates. “Pair” refers to galaxies with a close companion without any disturbed features. We do not know whether they are actual pairs or simply a line-of sight effect of physically separated galaxies. Though we classified these objects, we do not include them as interacting systems in this paper. The classification “accompanying Faint Companions” was proposed after the preliminary visual inspection of the overall populations of the galaxies. In this process, we found many galaxies accompanying faint dwarfish objects, mostly showing optical colors similar to those of the main galaxies. The small companions are usually extended along the radial direction to the center of the main galaxy or along the major axis of the galaxy. We classified them separately, suspecting that they are on-going minor merger systems or merger remnants capturing tidal dwarf galaxies that formed during the merger event of the past. Due to the ambiguity of identifying the systems, however, we did not include these galaxies in the analyses in this paper, too. Examples of the ‘PM’, ‘I’, ‘P’, ‘FC’ galaxies are presented in Figure 5. It should be noted that only PM and I samples are used in our analysis.

### 5.2. The result

Visual inspection was performed for the four Abell clusters following the scheme introduced in the previous subsection. In Table 5, we present the fractions of the post-merger (PM), interacting (I), pair (P) and faint companion (FC) galaxies among the  $RS_{sp}$  of each galaxy cluster. We found that the  $\sim 25 \pm 3\%$  of the  $RS_{sp}$  galax-

TABLE 5  
FRACTIONS OF THE POST-MERGER, INTERACTING, PAIR, AND FAINT COMPANION GALAXIES AMONG  $RS_{sp}$

ID	PM	I	P	FC
A119	27% (13/48)	0% (0/48)	10% (5/48)	10% (5/48)
A2670	28% (25/89)	8% (7/89)	3% (3/89)	6% (5/89)
A3330	22% (13/58)	5% (3/58)	9% (5/58)	3% (2/58)
A389	22% (17/78)	4% (3/78)	8% (6/78)	5% (4/78)
among the $RS_{sp}$ galaxies within $0.5R_{200}$				
A119	26% (8/31)	0% (0/31)	10% (3/31)	16% (5/31)
A2670	29% (18/63)	10% (6/63)	5% (3/63)	8% (5/63)
A3330	13% (4/30)	3% (1/30)	7% (2/30)	0% (0/30)
A389	23% (10/43)	5% (2/43)	12% (5/43)	7% (3/43)

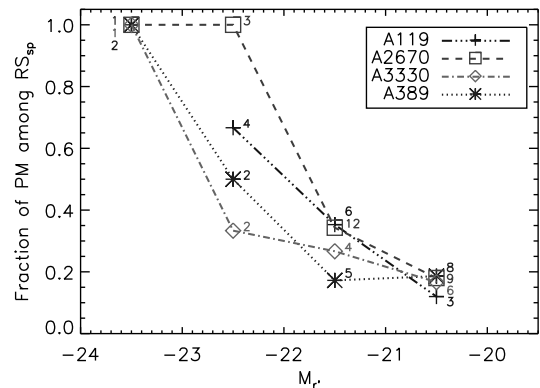


FIG. 6.— The fractions of post-merger galaxies are plotted along the absolute magnitudes. The numbers beside the points indicate the count of the PM galaxies used to derive the fractions. Although there is a large spread according to the small values for the bright galaxies, the overall tendency is consistent between all four target clusters. This figure shows that post-merger features are more common as red-sequence galaxies become brighter in a cluster environment.

TABLE 6  
A CATALOG OF POST-MERGER GALAXIES.

ID	RA	Dec	$r'$	$g' - r'$	B/T	$\mathcal{A}$	R (Mpc) <sup>a</sup>	$z$
a119sp-0	00:57:02.1	-00:52:31	13.52	0.73	0.84	0.539	1.324	0.044
a119sp-1	00:56:16.1	-01:15:19	13.65	0.74	0.98	0.399	0.000	0.044
a119sp-3	00:55:18.8	-01:16:38	13.78	0.74	...	0.185	0.746	0.044
a119sp-5	00:56:22.8	-01:12:35	13.88	0.66	0.54	0.425	0.167	0.049
a119sp-9	00:56:02.7	-01:20:04	14.33	0.74	0.68	0.178	0.301	0.042
a119sp-10	00:55:08.9	-01:02:47	14.48	0.72	0.73	0.149	1.087	0.045
a119sp-22	00:55:25.3	-01:18:32	14.96	0.61	0.67	0.154	0.680	0.041
a119sp-31	00:57:07.0	-01:23:50	15.11	0.73	0.71	1.143	0.794	0.048
a119sp-34	00:55:05.1	-01:15:09	15.23	0.68	0.47	1.035	0.921	0.043
a119sp-35	00:56:38.6	-01:23:26	15.23	0.69	0.56	0.406	0.512	0.043
a119sp-49	00:55:55.1	-01:03:51	15.61	0.70	0.41	0.994	0.655	0.044
a119sp-51	00:55:43.2	-01:02:01	15.69	0.66	0.29	0.593	0.811	0.042
a119sp-57	00:55:23.0	-01:12:40	15.76	0.68	0.26	0.486	0.703	0.042
a2670sp-0	23:54:13.7	-10:25:09	14.27	0.73	0.93	0.210	0.000	0.077
a2670sp-3	23:53:40.5	-10:24:20	15.14	0.67	0.92	0.271	0.718	0.073
a2670sp-5	23:53:47.6	-10:37:34	15.36	0.64	0.74	0.209	1.208	0.071
a2670sp-6	23:53:46.7	-10:16:15	15.44	0.59	0.62	0.523	0.961	0.079
a2670sp-15	23:54:05.7	-10:18:30	15.69	0.69	1.00	0.277	0.596	0.073
a2670sp-16	23:54:21.5	-10:25:11	15.77	0.70	0.59	0.430	0.168	0.076
a2670sp-21	23:53:32.7	-10:34:25	15.90	0.71	0.73	0.362	1.188	0.081
a2670sp-23	23:54:10.4	-10:29:51	15.99	0.67	0.77	0.316	0.412	0.075
a2670sp-25	23:54:14.8	-10:24:49	16.03	0.70	...	0.483	0.037	0.070
a2670sp-26	23:54:39.6	-10:25:23	16.01	0.71	0.68	0.628	0.558	0.077
a2670sp-34	23:53:56.0	-10:16:13	16.14	0.59	0.11	0.660	0.857	0.074
a2670sp-36	23:53:29.5	-10:31:43	16.16	0.65	0.38	1.126	1.106	0.073
a2670sp-38	23:54:01.4	-10:12:48	16.31	0.58	0.25	1.336	1.095	0.078
a2670sp-44	23:54:02.1	-10:25:59	16.40	0.61	0.75	0.556	0.259	0.071
a2670sp-51	23:53:24.0	-10:08:51	16.45	0.66	1.00	0.914	1.764	0.075
a2670sp-53	23:54:17.1	-10:24:56	16.45	0.72	0.75	0.270	0.077	0.081
a2670sp-75	23:54:30.8	-10:13:24	16.72	0.56	0.84	0.390	1.075	0.076
a2670sp-78	23:54:14.9	-10:14:09	16.78	0.67	0.44	0.319	0.946	0.075
a2670sp-79	23:53:20.0	-10:32:16	16.84	0.57	0.25	0.614	1.308	0.074
a2670sp-88	23:54:10.1	-10:24:25	16.93	0.69	0.98	0.459	0.099	0.080
a2670sp-103	23:53:48.4	-10:24:54	17.12	0.67	0.58	0.580	0.545	0.080
a2670sp-114	23:54:51.9	-10:28:08	17.26	0.57	0.69	0.253	0.861	0.080
a2670sp-141	23:54:19.6	-10:25:54	17.38	0.61	0.75	0.214	0.143	0.074
a2670sp-142	23:54:13.3	-10:07:13	17.39	0.61	0.07	1.332	1.543	0.076
a2670sp-146	23:53:26.8	-10:24:42	17.41	0.53	0.00	1.181	1.009	0.072
a3330sp-0	05:14:39.5	-49:03:29	14.23	0.72	0.91	0.549	0.000	0.091
a3330sp-5	05:16:06.0	-48:53:58	15.64	0.73	0.59	0.747	2.354	0.092
a3330sp-7	05:14:29.4	-49:05:53	15.73	0.74	0.60	0.289	0.347	0.090
a3330sp-26	05:15:29.5	-49:03:45	16.43	0.70	0.71	0.969	1.246	0.086
a3330sp-46	05:15:44.3	-48:53:33	16.81	0.64	0.77	0.679	1.894	0.091
a3330sp-47	05:16:03.3	-49:14:23	16.81	0.66	0.67	1.178	2.353	0.092
a3330sp-52	05:14:46.4	-49:04:41	16.84	0.76	0.13	0.322	0.209	0.087
a3330sp-55	05:16:10.5	-48:53:23	16.92	0.70	0.26	0.369	2.482	0.087
a3330sp-57	05:14:38.3	-49:01:44	16.95	0.76	0.50	0.195	0.177	0.090
a3330sp-68	05:14:47.2	-48:45:31	17.03	0.70	0.48	0.295	1.802	0.089
a3330sp-69	05:15:17.2	-49:03:51	17.06	0.62	0.24	0.951	0.941	0.088
a3330sp-99	05:16:09.4	-48:54:30	17.41	0.67	0.44	1.240	2.412	0.088
a3330sp-100	05:14:22.3	-49:14:54	17.40	0.73	1.00	1.006	1.215	0.087
a389sp-0	02:51:32.7	-25:04:23	14.80	0.76	0.70	0.286	0.978	0.113
a389sp-1	02:51:24.8	-24:56:39	15.08	0.69	0.76	0.283	0.000	0.112
a389sp-6	02:51:46.4	-24:51:09	15.87	0.74	0.87	1.207	0.945	0.110
a389sp-11	02:51:34.7	-25:02:44	16.25	0.66	0.77	1.670	0.806	0.116
a389sp-16	02:50:44.9	-24:45:42	16.46	0.64	0.78	1.199	1.814	0.115
a389sp-19	02:50:54.1	-24:45:24	16.58	0.73	0.13	0.893	1.669	0.117
a389sp-21	02:51:59.2	-24:52:31	16.60	0.62	0.00	1.104	1.170	0.109
a389sp-23	02:51:13.2	-24:56:50	16.64	0.59	...	0.596	0.355	0.110
a389sp-61	02:50:43.7	-25:00:11	17.27	0.55	0.07	0.941	1.332	0.116
a389sp-70	02:50:59.6	-24:54:27	17.35	0.64	0.51	0.651	0.818	0.112
a389sp-73	02:51:22.1	-24:53:27	17.39	0.63	0.12	0.826	0.401	0.109
a389sp-82	02:51:20.0	-24:53:14	17.40	0.65	0.64	1.024	0.443	0.117
a389sp-112	02:51:40.8	-24:49:30	17.71	0.59	0.61	0.466	1.004	0.114
a389sp-163	02:50:26.9	-24:49:20	18.04	0.64	0.87	0.970	1.988	0.109
a389sp-175	02:51:22.5	-25:07:41	18.13	0.52	1.00	1.061	1.354	0.116
a389sp-207	02:50:44.3	-24:55:22	18.26	0.66	0.05	1.029	1.249	0.108
a389sp-217	02:51:27.6	-24:56:40	18.28	0.72	0.19	0.429	0.086	0.108

<sup>a</sup> A projected distance of a galaxy from the BCG in each galaxy cluster.



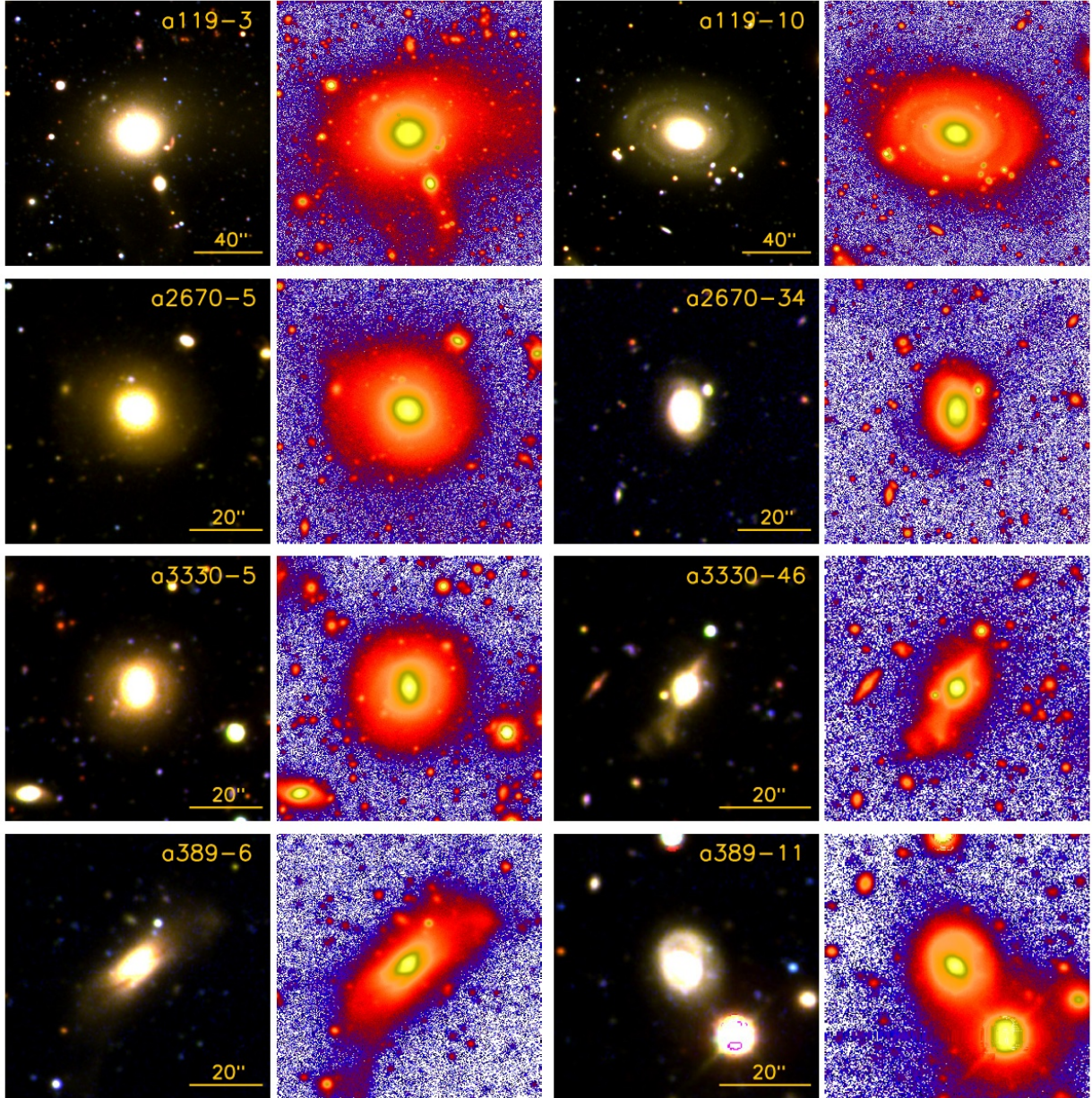


FIG. 7.— Post-merger galaxy samples from four Abell clusters. The first column of each galaxy is a pseudo-color image generated with  $u'g'r'$  deep images. The second column is a surface brightness map of the galaxy, revealing faint features which do not appear in the color image.

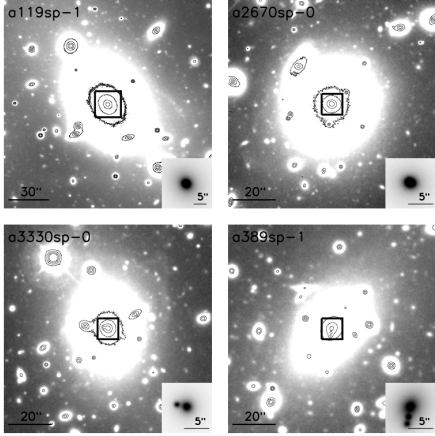


FIG. 8.— The BCGs in our cluster samples are presented with  $r'$  band deep images. The contours are drawn for  $\mu_{r'} = 19, 20, 21, 22 \text{ mag/arcsec}^2$ . The inset image in right bottom corner of each galaxy shows the central region indicated by a rectangle box in each image. A119, A2670 and A3330 showed faint structures in their halos. Moreover, A3330 and A389 revealed multiple cores in their centers. This implies that even the BCGs continued violent galaxy mergers until the recent epoch.

ies exhibit post-merger signatures in the galaxy clusters at  $z \lesssim 0.1$ . The fractions of the other classes were usually less than 10% for each class. If we consider post-mergers and interacting galaxies together, the fractions of the disturbed galaxies will be 27%, 36%, 28%, and 26% respectively in A119, A2670, A3330 and A389. On average, the fraction of galaxies related to recent galaxy mergers is  $\sim 30 \pm 4\%$  in the clusters at  $z \lesssim 0.1$ .

The FOVs of the MOSAIC 2 deep images do not cover the entire area within  $R_{200}$  for A119 and A2670, as demonstrated in Section 4.1. Therefore, we derived the fractions again with the  $RS_{sp}$  galaxies located within  $0.5R_{200}$  of each galaxy cluster. The results are presented in the bottom half of Table 5. Although we applied more consistent areas of clusters, the result did not differ much from the previous one. The fraction of post-merger galaxies within  $0.5R_{200}$  was  $\sim 24 \pm 4\%$  on average. The value slightly lower than that ( $\sim 25 \pm 3\%$ ) in the previous sample is most likely a result of A3330 showing a distinctively low post-merger fraction within the half of  $R_{200}$ .

While most of the fractions in a certain class show similar values between the clusters, it is interesting that no interacting galaxies were found among the bright red-sequence galaxies of A119. This may have been affected by the relatively small sky coverage of A119 ( $\sim 0.6R_{200}$ ) by the MOSAIC 2 deep images. Because galaxy interactions would be more plausible at cluster outskirts, it is possible that we missed some galaxies out of the FOV. Another possible reason is that A119 is the smallest galaxy cluster among our target clusters and therefore includes fewer bright galaxies. The derived size and mass of the clusters are presented in Table 4. If we assume that the fraction of interacting galaxies within  $0.5R_{200}$  of A119 may be similar to the value for A3330 ( $\sim 3\%$ ), which is the second smallest galaxy cluster among the clusters, we expect only  $\lesssim 1$  galaxies within the area. Therefore, there is a very low chance to find the bright interacting galaxies in the given FOV of the A119 data.

The fractions of post-merger (PM) galaxies are plotted along the absolute magnitudes in Figure 6. The numbers beside the data points indicate the counts of PM galaxies used to derive the fractions. Although there is a large spread according to the small values for the bright galaxies, the overall tendency is consistent between all four target clusters. This figure shows that post-merger features are more common in bright red-sequence galaxies in a cluster environment.

Samples of the selected post-merger galaxies are presented in Figure 7. In this figure, the first column of each galaxy image set is a pseudo-color image generated with  $u'g'r'$  deep images. The second column is a  $r'$  band surface brightness map of the galaxy revealing faint features which do not appear in the pseudo-color images due to the luminous galactic centers.

In fact, the BCGs in all four target clusters revealed extended faint features or multiple nuclei in our deep images. We present four BCGs separately in Figure 8 with their  $r'$  band deep image and the surface brightness contours. The inset images show the center of the BCGs indicated by the rectangle boxes. A119, A2670 and A3330 BCGs showed faint structures in their halos. In addition to that, A3330 and A389 BCGs revealed multiple cores in their centers. This implies that even the BCGs continued violent galaxy mergers until the recent epoch.

We provide a catalog of the post-merger galaxies in Table 6 with their observational properties.

## 6. MORPHOLOGICAL EXAMINATION

### 6.1. Bulge-to-total ratios and residual images

Galaxy bulge-to-total ratios (B/T) were measured for the spectroscopic members of the galaxy clusters. Ratios are derived from the radial surface brightness profiles of the galaxies, as measured by the `ellipse` task in IRAF. Because the cores of bright galaxies are usually saturated in the deep images, we merged the two profiles from the shallow image and the deep image for the central part and the outer part of a galaxy, respectively. The conjunction is made at the radius where both profiles show the same surface brightness.

We found the best fits of the galaxy profiles to the composite galaxy model of the de Vaucouleurs profile (Sersic index,  $n = 4$ ) and the exponential profile. The galaxy surface brightness model can be expressed as,

$$I(R) = I_e \exp(c \times ((R/R_e)^{1/4} - 1)) + I_d \exp(-R/R_d). \quad (5)$$

Here,  $R_e$  is the effective radius of the de Vaucouleurs profile and  $I_e$  is the surface brightness at  $R_e$ . The constant,  $c$ , is set as a free parameter to be determined.  $R_d$  is the disk scale length and the  $I_d$  is the surface brightness at  $R_d$ . The fitting is performed using the IDL routines in the MPFIT package (Markwardt 2008). Usually such a fitting procedure is very sensitive to the initial values of the fitting parameters. To increase the success rate of the fitting, galaxy profiles are fitted with the de Vaucouleurs profile first. The preliminarily derived values of  $I_e$ ,  $R_e$  and  $c$  are then used as an initial guess for the more complex main fitting with the equation (5) and all the parameters are determined again as well as  $I_d$  and  $R_d$ . The galaxy B/T is calculated using the following formula:

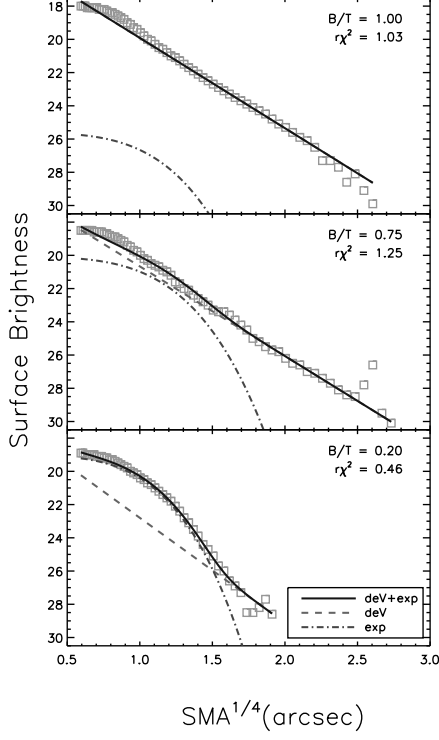


FIG. 9.— Galaxy radial profiles and the fitting results are presented. The open rectangles indicate that the ellipsoid is fitted successfully for the annulus by the `ellipse` task. The best fit of the surface brightness profile is depicted using solid lines over the data points. The de Vaucouleurs profile and the exponential profile comprising the best fit are also presented, in dashed lines and dashed-dotted lines, respectively. This figure shows that the galaxy profiles are robustly measured to  $\mu_{r'} \sim 30$  mag/arcsec.

$$B/T = \frac{R_e^2 I_e}{R_e^2 I_e + 0.28 R_d^2 I_d} \quad (6)$$

We present examples of the galaxy profile fitting in Figure 9. The best fit of the surface brightness profile is drawn over the data points using the parameters derived from the fitting. The de Vaucouleurs profile and the exponential profile comprising the best fit are also presented. The figure shows that the galaxy profiles are robustly measured to  $\mu_{r'} \sim 30$  mag/arcsec.

Figure 10 shows the result of B/T calculations for the cluster members. In the upper panel of each graph set, galaxies are expressed in different colors along their B/T values in the optical CMR. The high values of B/T of bright red-sequence galaxies and the low values of blue galaxies are consistent with the general expectation. In the bottom panels, average B/T values for  $RS_{sp}$  are plotted along the absolute magnitude. As the upper panels have already suggested, it was found that the average B/T becomes smaller as the galaxies become fainter.

We also computed the averages for the post-merger galaxies separately and presented them in red filled circles with the standard deviations. The results indicate that the average B/T values for post-merger galaxies are slightly higher than the average of the rest of the  $RS_{sp}$  galaxies in the magnitude range.

We classified galaxies with  $B/T > 0.4$  as ellipticals and S0s following the criteria applied in Somerville & Pri-

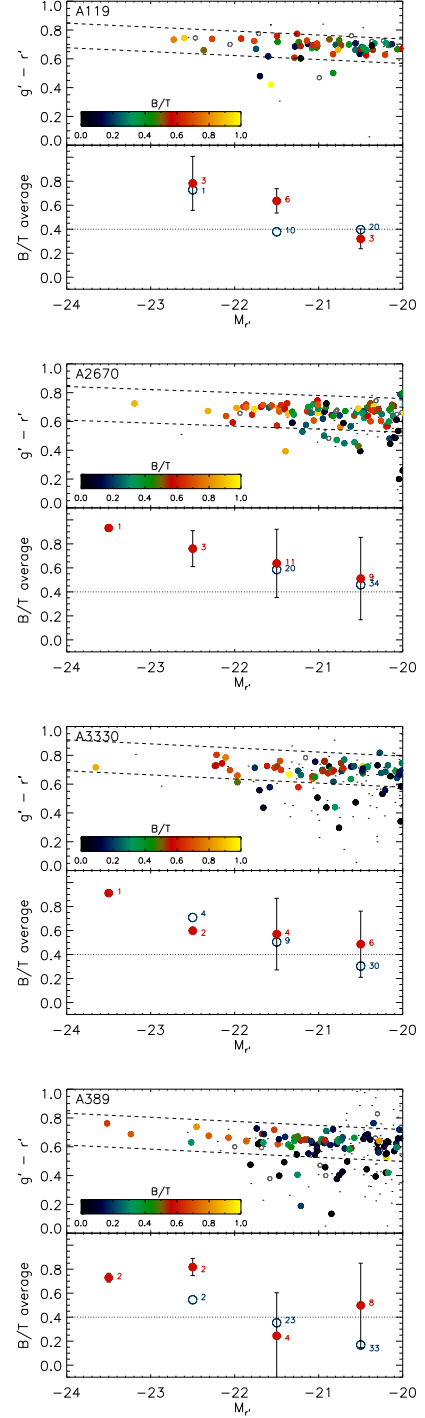


FIG. 10.— The derived B/T values are presented for the spectroscopic member galaxies brighter than  $M_{r'} = -20$  in each galaxy cluster. *upper:* The B/T are expressed with color-coded filled circles in the optical CMR of each galaxy cluster. The dashed lines indicate color ranges of the red-sequence galaxies. The graphs confirm that bright red-sequence galaxies are mostly bulge-dominated systems with large B/T values while the blue galaxies show small B/T values uniformly. *bottom:* The averages B/T of post-merger galaxies among  $RS_{sp}$  galaxies are plotted along the magnitude with the red-filled circles. The error bars show standard deviations of the mean values. Blue open circles are the average B/T of  $RS_{sp}$  galaxies except the PM galaxies, presented for comparison. The number of galaxies counted for each average value is indicated beside the data point. We demarcate  $B/T = 0.4$  in the plots with the dotted lines, with which E/S0 galaxies are distinguished from spirals in this work. The graphs indicate that most of PM galaxies are bulge-dominated E/S0 galaxies.



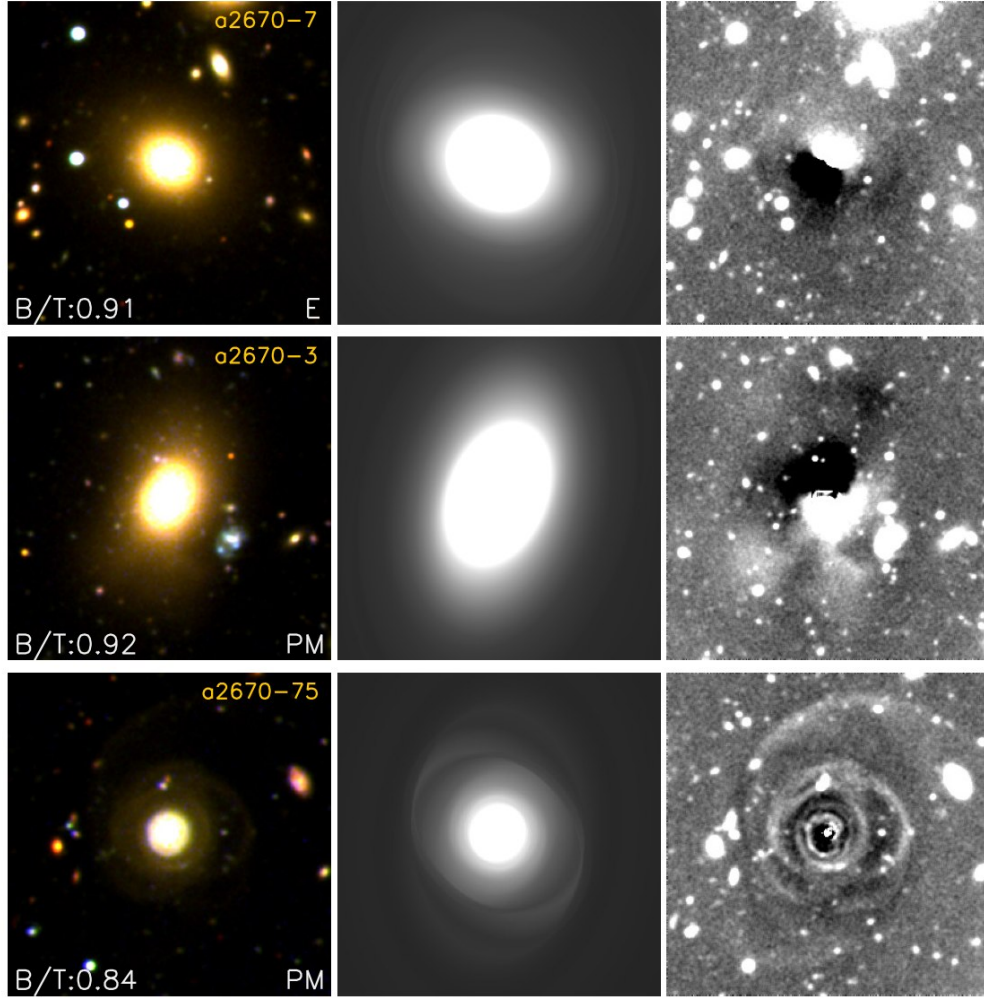


FIG. 11.— Pseudo-color images, two-dimensional galaxy models and model-subtracted residual images of galaxies are presented from left to right in the same scale for each galaxy. The images of an early-type galaxy are presented in the top panels for comparison. The residual in the middle panel shows an example of discontinuous (in other words, structured) halo of an early-type galaxy while the bottom panel exhibits an obvious merger remnant with a long tidal tail and the spiral structures.

mack (1999). The results show that a large fraction of the featured galaxies are bulge-dominated systems as 77% (10/13), 72% (18/25), 77% (10/13) and 59% (10/17) for A119, A2670, A3330, and A389, respectively. This implies that possible contamination from disturbed spirals is not significant in our visual inspection. As a result, the fractions of post-merger galaxies among the bulge-dominated systems ( $B/T > 0.4$ ) are about 40% (10/25), 34% (18/53), 36% (10/28) and 48% (10/21) for A119, A2670, A3330, and A389, respectively. On average, it is  $38 \pm 5\%$  in our cluster sample. If we apply a more strict  $B/T$  criterion for bulge-dominated systems as  $B/T > 0.6$ , the average of post-merger galaxy fractions increases to  $46 \pm 8\%$ .

Two-dimensional galaxy surface brightness models are constructed with the result of `ellipse` fitting and are subtracted from the deep images in order to check the features of the post-merger galaxies. The residual images of three  $RS_{sp}$  galaxies with similar  $B/T$  values are shown in Figure 11. At the same time, the images of three

galaxies demonstrate the robustness of our  $B/T$  calculation for early-type galaxies. Pseudo-color images, two-dimensional galaxy models and model-subtracted residual images are presented from left to right. An image of an early-type galaxy is presented in the top panels for comparison. Middle and bottom panels show examples of post-merger galaxies showing asymmetric, disturbed structures in their residual images.

### 6.2. Asymmetry

Using the  $r'$  band deep images, we measured the asymmetry index,  $\mathcal{A}$  for the cluster members. The measurements were made within the area between  $0.5R_{Petro}$  and  $2R_{Petro}$  of each galaxy avoiding galaxy centers usually saturated.

The  $\mathcal{A}$  can be expressed as,

$$\mathcal{A} = \frac{\sum_{i,j} |I(i,j) - I_{180}(i,j)|}{\sum_{i,j} |I(i,j)|} \quad (7)$$

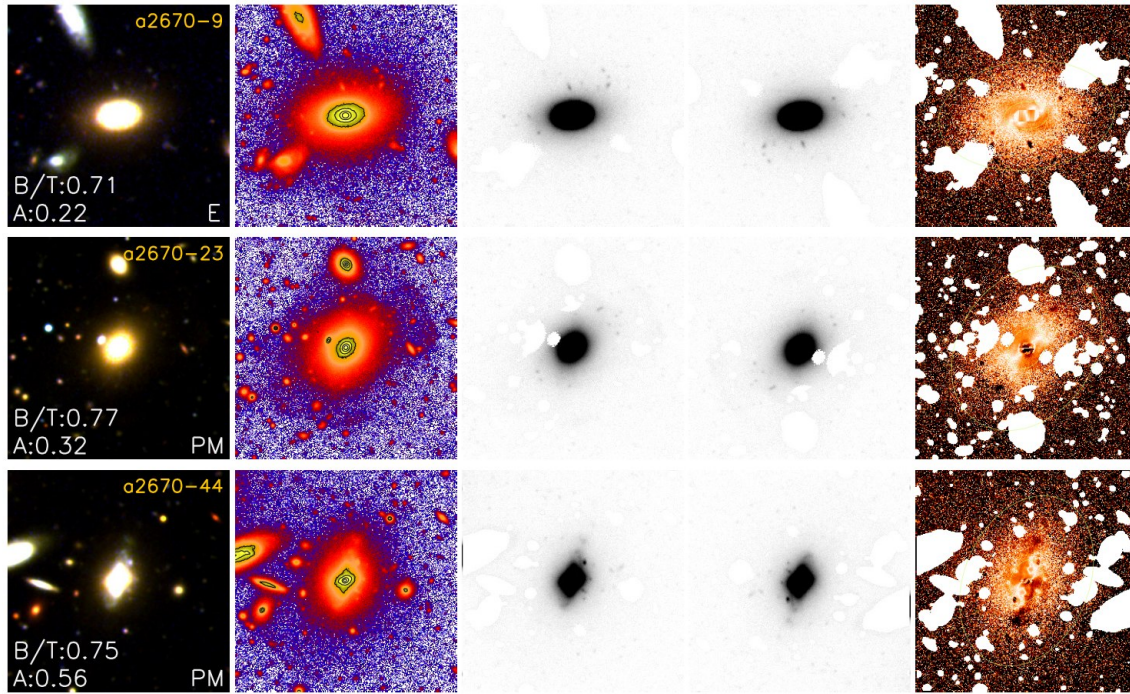


FIG. 12.— Asymmetry. A color composite image (first), surface brightness map (second), r band deep image (third), the same deep image rotated 180 degrees (fourth), and a normalized residual image (fifth). The green ellipses in the last column indicate  $0.5R_{\text{Petro}}$  and  $2R_{\text{Petro}}$  of each galaxy in which  $\mathcal{A}$  was measured.

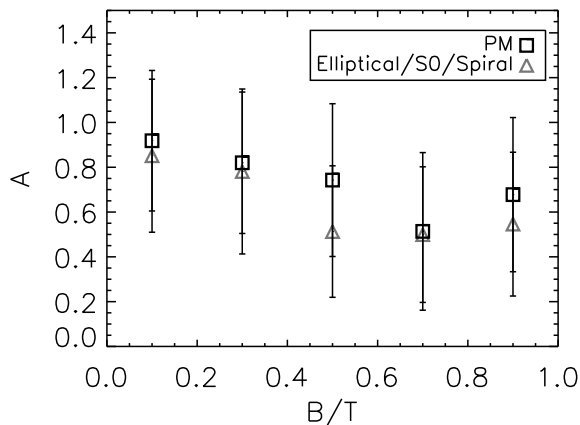


FIG. 13.— Asymmetry distribution of red-sequence member galaxies along their B/T. Compared to normal elliptical and spiral galaxies, PM galaxies showed a slightly larger  $\mathcal{A}$  on average.

where  $I$  is an original image and the  $I_{180}$  is the image rotated by  $180^\circ$ . We demonstrate the calculation process with some examples of  $RS_{sp}$  galaxies showing similar B/T values in Figure 12. The first column shows pseudo-color images and the second one displays  $r'$  band surface brightness map of the galaxies. The third and fourth images show the original deep image and the same image rotated 180 degrees. The rotated images are subtracted from the original images and the normalize by the original images. The last column presents the normalized residual images with green ellipses indicating  $0.5R_{\text{Petro}}$  and  $2R_{\text{Petro}}$  of each galaxy in which the  $\mathcal{A}$  was measured.

Prior to the calculations, all nearby objects around the galaxies were masked from the images as shown in the images with white masks.

The average  $\mathcal{A}$  of normal elliptical and spiral galaxies and the post-merger galaxies are plotted along their B/T values in Figure 13. While the figure confirms that late-type galaxies show large asymmetry values compared to early-type galaxies on average. Although the result corresponds to simple expectation, however, the averages of  $\mathcal{A}$  contain a large spread of the values as expressed with error bars in the figure. We suppose that the post-merger features in such a faint surface brightness level of our  $r'$  band data were not easily recognizable with the asymmetry index,  $\mathcal{A}$ .

## 7. DISCUSSION

We investigated the post-merger signatures of red-sequence galaxies in rich Abell clusters at  $z \lesssim 0.1$ . Deep images in  $u'$ ,  $g'$ ,  $r'$  and medium-resolution galaxy spectra were taken for A119, A2670, A3330 and A389 with a MOSAIC 2 CCD and a Hydra MOS mounted on the Blanco 4-m telescope at CTIO. Post-merger signatures were identified by visual inspection of their disturbed features, e.g., asymmetric structures, faint features, discontinuous halo structures, rings and dust lanes. Most ( $\sim 71\%$ ) of the featured galaxies were found to be bulge-dominated systems (E/S0 galaxies) from the radial surface brightness profile fitting. On average, the asymmetry of the post-merger galaxies is always slightly larger than the mean of normal galaxies within the same bulge-

TABLE 7  
COMPARISONS BETWEEN CLUSTER AND FIELD

	Class	Cluster	Field <sup>a</sup>
Red <sup>b</sup>	PM	25 ± 3%	35%
	I	5 ± 1%	18%
	Total	30 ± 4%	53%
Bulge-dominated <sup>c</sup>	PM	38 ± 5%	49%
	I	4 ± 1%	21%
	Total	42 ± 6%	70%

<sup>a</sup> The fractions for the field environment were adopted from van Dokkum (2005).

<sup>b</sup> Fractions for the cluster are derived with the  $RS_{sp}$  galaxies in this paper, while the field red galaxies are denoted with  $B - R$  colors.

<sup>c</sup> Fractions with only bulge-dominated galaxies among the red galaxies. For the cluster, galaxies with  $B/T > 0.4$  are included while visually classified E/S0 galaxies are considered for the field.

to-total ratio range.

We noted that cluster red-sequence galaxies went through galaxy mergers until the recent epoch. In this work,  $\sim 25\%$  of the bright ( $M_r < -20$ ) cluster red-sequence ( $RS_{sp}$ ) galaxies exhibited post-merger signatures in four target clusters consistently. The fraction increases to  $\sim 38\%$  with the bulge-dominated  $RS_{sp}$  galaxies ( $B/T > 0.4$ ). In addition, brighter galaxy samples show higher fractions of post-merger signatures in the clusters.

In Table 7, we compared the average of fractions from the four Abell clusters with the result of field environment from van Dokkum (2005). The clusters and field environments were compared using two subsets of galaxy samples, red galaxies and bulge-dominated red galaxies. Our  $RS_{sp}$  galaxies were compared with the luminous red galaxies selected using  $B - R$  colors in van Dokkum (2005), and the bulge-dominated galaxies ( $B/T > 0.4$ ) were compared with the visually classified field E/S0 galaxies in the same paper. We presented the fractions of post-merger galaxies and interacting galaxies separately as well as the combined fractions which indicate the fraction of disturbed galaxies related to past or ongoing galaxy mergers. The van Dokkum sample does come with spectroscopic redshift; spectroscopic redshifts were available only on 5 galaxies out of 126 and so no k-correction was applied. Based on a small subsample he argues that his galaxies are roughly at redshift of 0.1, which is comparable to ours. The colors of his bulge-dominated galaxies are also comparable to ours after proper color conversions using Lupton (2005).

The table demonstrates that the overall fractions in clusters are lower than those in the field. We find it difficult to understand the “interacting” galaxies in these clusters. They appear to be beginning their interaction/merger, and so we classified them as “interacting” or pre-merger. Considering that interacting systems with small companions are likely missed in our search, it is likely that our fraction for interacting galaxies is a hard lower limit. For example, some of our “faint companion galaxies” (which were excluded in our analysis) could be “interacting”. Direct satellite-satellite mergers are supposed to be extremely rare in large halo environments, and so it is difficult to understand them.

The fractions of post-merger galaxies are not very dif-

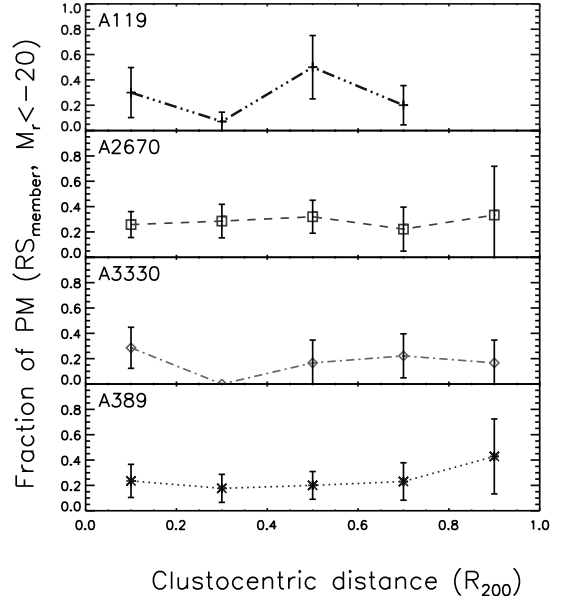


FIG. 14.— Fractions of PM galaxies along the projected distances from the BCGs. The size of distance bin is  $0.2R_{200}$  in each galaxy cluster. Contrary to the general assumption, which would predict more frequent mergers at the outskirts of a cluster, the fraction of PM galaxies does not change much along the clustocentric distances.

ferent between the cluster and the field. This is not compatible with a simple theoretical expectation based on merger timescale as a function of relative speeds of galaxies. Therefore, we suggest that many massive red-sequence galaxies formed in a less dense environment through galaxy mergers and entered into the cluster through dark matter halo mergers.

An important caveat exists on this comparison between van Dokkum’s work and ours. Merger timescales and thus probability heavily depends on mass ratio of colliding systems, but it is very difficult to extract the mass ratio information from observed images. We thought it would be the best attempt to use similar instruments for similar depth (exposure) on galaxies at similar distances. But even in this case, we are not free from a possible environmental (cluster vs field) dependence on mass ratios of galaxy mergers.

The radial distribution of the post-merger galaxies in the clusters provides another hint supporting this scenario. The fractions of post-merger galaxies are derived along the projected distance from the BCG in the scale of  $R_{200}$  of each galaxy cluster, as shown in Figure 14. We found that the fractions do not change much along the clustocentric distances. In situ mergers can scarcely explain this result because it is difficult to expect frequent mergers in the central region of clusters compared to the outskirts. This implies again that a large fraction of massive red-sequence galaxies with post-merger signatures likely merged in a less dense environment and then fell into the central region of the cluster.

Is it possible for a galaxy to maintain the post-merger features produced in the outskirts until the galaxy arrives at the cluster center? It has been suggested for a long time that tidally ejected materials during galaxy mergers may return over many Gyr (Hernquist & Spergel 1992; Hibbard & Mihos 1995). Lotz et al. (2008) also proposed

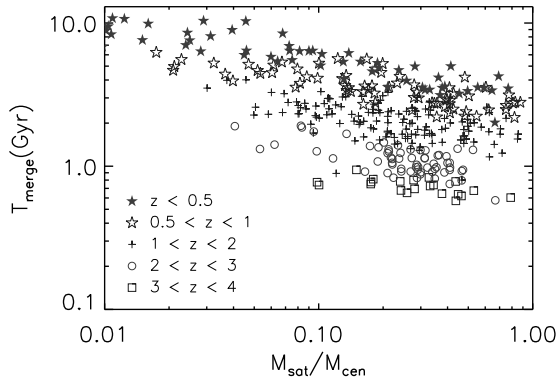


FIG. 15.— Merging timescale of galaxies in a cluster of  $5 \times 10^{14} M_{\odot}$  of our SAM along the mass ratio. If we assume that a central galaxy is the BCG, bright satellite galaxies ( $M_{\text{sat}} > 0.25 M_{\text{cen}}$ ) merge into the BCG within  $\sim 4$  Gyr at  $z < 0.5$ .

that the features of interacting galaxies can be observable for up to  $\sim 2$  Gyr by applying stellar population models to the simulated equal-mass gas-rich disc mergers. We note that the duration of merger feature is highly sensitive to galaxy type, merger geometry, mass ratio, and last but not least the observing surface brightness limit<sup>1</sup>.

The dynamical friction timescale of a satellite galaxy to the central cluster halo would be another parameter to compare with the observable timescale of post-merger features. In this work the dynamical friction timescale is defined as the timescale between the epochs of when the halo of satellite galaxy is started to merge into the cluster halo at the cluster virial radius and when the satellite galaxy have finally merged into the BCG in the model. If a dynamical friction timescale for a galaxy is much longer than the timescale of the post-merger features, our results should be interpreted in a different light. By taking advantage of a semi-analytic approach, we obtained the relationship between the merger mass ratio and the merger timescale of galaxies to the BCG. Our semi-analytic model (SAM) is based on N-body backbone dark matter merger trees and physical ingredients that govern the baryonic properties of galaxies. The merger timescales in the model are calculated using the formulae of Jiang et al. (2008), which provides a modified form of Chandrasekhar's formula. Given that Chandrasekhar's formula generally underestimates merger timescales, Jiang et al. (2008) fits the formula into merger timescales derived from hydrodynamic simulations (see also Kimm, Yi, & Khochfar 2011).

We selected a cluster in the model which has a cluster mass,  $5 \times 10^{14} M_{\odot}$ , comparable to our cluster samples. Figure 15 shows the merging timescales of all satellite galaxy mergers along the mass ratio between the BCG and the satellite, consequently forming a cluster of  $5 \times 10^{14} M_{\odot}$  at present. The redshift of each merger was expressed using different symbols, showing that the merger timescale was shorter at a higher redshift for the same mass ratio in the model. This arises because the size of the cluster was smaller at an early epoch. We can

<sup>1</sup> The suggestion of 2 Gyr visibility of merger features by Lotz et al. (2008) was based on the surface brightness,  $\mu = 25$  assumption. The visibility time is likely longer in our case because our imaging was deeper.

assume that the oldest observable post-merger features in our target clusters are produced at  $z \sim 0.5$ , where the difference in the lookback time from  $z \sim 0.1$  is about 4 Gyr. The figure shows that the dynamical friction timescale of a satellite galaxy as massive as  $M_{\text{sat}}/M_{\text{cen}} > 0.25$  will be  $\lesssim 4$  Gyr below the redshift,  $z = 0.5$ . If we assume that the magnitude difference between the BCG and the second BCG is 1 magnitude, then the mass ratio would be  $\sim 0.4$  ( $M_{\text{sat}}:M_{\text{cen}} = 1:2.5$ ). The figure indicates that then the second BCG will merge into the BCG within 3 Gyr at  $z < 0.5$ . Therefore, it appears that massive post-merger galaxies can fall into the cluster center and maintain their disturbed features, even in low redshift ( $z < 0.5$ ). The consistent fractions of the featured galaxies along the clustocentric distance most likely arise from on-going halo mergers which started during various epochs.

The average count of post-merger galaxies in our cluster samples was  $17 \pm 6$  galaxies (13, 25, 13 and 17 galaxies for A119, A2670, A3330 and A389, respectively). We also counted the number of halo mergers related to the current cluster halo in the SAM, to check whether a cluster can experience sufficient halo mergers to absorb massive galaxies since  $z = 0.5$ . In the model of a  $5 \times 10^{14} M_{\odot}$  cluster, we found 21 satellite halos merging into the cluster at  $z < 0.5$ , with galaxies brighter than  $M_r' = -20$ . It theoretically supports that a massive cluster may have enough halo mergers to take recently merged galaxies in at recent epoch. In this preliminary analysis, we assumed that merger features from the previous halo environment last roughly the same time as the subhalo's dynamical friction timescale. This is certainly an oversimplification. A more realistic calculation would require accurate merging halo mass ratios, merging galaxy mass ratios, and merger feature timescales throughout cluster evolution history.

In conclusion, we found that  $\sim 42\%$  of massive, bulge-dominated red-sequence galaxies in galaxy clusters have continued their mass assembly through galaxy mergers until the recent epoch, as  $\sim 70\%$  of the field galaxies have done. Although the fractions of post-merger galaxies in clusters are lower than that in the field, it is still too high compared to the expectation from apparent fractions of galaxy interaction in galaxy clusters. Therefore, we propose that most of those post-merger galaxies were assembled in a low-density region and fell into the current cluster via halo mergers. We have supported this scenario with theoretical predictions using a semi-analytical model.

We do not speculate the progenitors of the post-merger galaxies in this paper, regardless of whether they are remnants of dry mergers or wet mergers. This will be investigated in depth in an upcoming paper which will discuss on the ultraviolet properties of the galaxies most likely related to the residual star formation induced by galaxy mergers.

We thank Yujin Yang for helping us obtain the short exposure images of Abell 389. Y. -K. Sheen is grateful to Knut Olsen, Francisco Valdes and Mike Fitzpatrick for their helpful comments and discussions on the MOSAIC 2 and Hydra data. We acknowledge the support from the

National Research Foundation of Korea to the Center for Galaxy Evolution Research and Doyak grant (No. 20090078756) and from the Korea Astronomy and Space

Science Institute.

*Facilities:* MOSAIC 2, Hydra (CTIO)

#### REFERENCES

- Bell, E. F., Wolf, C., Meisenheimer, K., et al. 2004, *ApJ*, 608, 752
- Bertin, E., & Arnouts, S. 1996, *A&AS*, 117, 393
- Bower, R. G., Lucey, J. R., & Ellis, R. S. 1992, *MNRAS*, 254, 601
- Bundy, K., Fukugita, M., Ellis, R. S., et al. 2009, *ApJ*, 697, 1369
- Carlberg, R. G., Yee, H. K. C., & Ellingson, E. 1997, *ApJ*, 478, 462
- de Ravel, L., Le Fèvre, O., Tresse, L., et al. 2009, *A&A*, 498, 379
- Dressler, A. 1980, *ApJ*, 236, 351
- Drory, N., & Alvarez, M. 2008, *ApJ*, 680, 41
- Faber, S. M., Willmer, C. N. A., Wolf, C., et al. 2007, *ApJ*, 665, 265
- Gunn, J. E., & Gott, J. R. 1972, *ApJ*, 176, 1
- Hernquist, L., & Spergel, D. N. 1992, *ApJ*, 399, L117
- Hibbard, J. E., & Mihos, J. C. 1995, *AJ*, 110, 140
- Jannuzi, B. T., Claver, J., & Valdes, F. 2003, “The NOAO Deep Wide-Field Survey MOSAIC Data Reduction” (<http://www.noao.edu/noao/noaodeep/ReductionOpt/frames.html>)
- Jiang, C. Y., Jing, Y. P., Faltenbacher, A., Lin, W. P., & Li, C. 2008, *ApJ*, 675, 1095
- Kang, E., & Im, M. 2009, *ApJ*, 691, L33
- Kaviraj, S., Schawinski, K., Devriendt, J. E. G., et al. 2007, *ApJS*, 173, 619
- Kaviraj, S., 2010a, *MNRAS*, 406, 382
- Kaviraj, S., 2010b, *MNRAS*, 408, 170
- Kimm, T., Yi, S. K., & Khochfar, S. 2011, *ApJ*, 729, 11
- Kodama, T., Tanaka, I., Kajisawa, M., et al. 2007, *MNRAS*, 377, 1717
- Lotz, J. M., Jonsson, P., Cox, T. J., & Primack, J. R. 2008, *MNRAS*, 391, 1137
- Lupton, R. 2005, “Transformation between SDSS magnitudes and  $UBVR_cI_c$ ” (<http://www.sdss.org/dr7/algorithms/sdssUBVRITransform.html#Lupton2005>)
- Markwardt, C. B. 2008, ASP conference series, Vol. 411, p. 251
- Schlege, D. J., Finkbeiner, D. P., & Davis, M. 1998, *ApJ*, 500, 525
- Smith, J. A., Tucker, D. L., Allam, S. S., & Rodgers, C. T. 2003, *AJ*, 126, 2037
- Somerville, R. S., & Primack, J. R. 1999, *MNRAS*, 310, 1087
- Stanford, S. A., Eisenhardt, P. R., & Dickinson, M. 1998, *ApJ*, 492, 461
- Tanaka, M., Kodama, T., Arimoto, N., et al. 2005, *MNRAS*, 362, 268
- Tonry, J., & Davis, M. 1979, *AJ*, 84, 1511
- Valdes, F. 2000, “Creating a Mosaic World Coordinate System” (<http://iraf.noao.edu/projects/ccdmosaic/astrometry/astrom.html>)
- van Dokkum, P. G. 2001, *PASP*, 113, 1420
- van Dokkum, P. G. 2005, *AJ*, 130, 2647
- Yi, S. K., Lee, J., Sheen, Y. -K., et al. 2011, *ApJS*, 195, 22